Soft Matter

Coarse-grained Molecular Dynamics Simulations of Slide-ring Gels under Finite Deformation: Influence of Sliding Ring Rearrangement on Softness and Extensibility

Journal:	*Soft Matter*
Manuscript ID	SM-ART-01-2025-000003.R2
Article Type:	Paper
Date Submitted by the Author:	17-Mar-2025
Complete List of Authors:	Yasuda, Yusuke; Kansai University, Organization for Research and Development of Innovative Science and Technology (ORDIST) Masumoto, Takeyoshi; The University of Tokyo Graduate School of Frontier Sciences Koichi, Mayumi; The University of Tokyo, Advanced Materials Science Toda, Masatoshi; National Institute of Advanced Industrial Science and Technology Tsukuba Yokoyama, Hideaki; The University of Tokyo, Morita, Hiroshi; National Institute of Advanced Industrial Science and Technology Tsukuba Ito, Kohzo; University of Tokyo, Department of Advanced Materials Science

Coarse-grained Molecular Dynamics Simulations of Slide-ring Gels under Finite Deformation: Influence of Sliding Ring Rearrangement on Softness and Extensibility

Yusuke Yasuda,[*,1] Takeyoshi Masumoto,[2] Koichi Mayumi,[*,3,4] Masatoshi Toda,[5] Hideaki Yokoyama,[2, 3] Hiroshi Morita,[5] Kohzo Ito[*, 2, 3]

[1]Organization for Research and Development of Innovative Science and Technology (ORDIST), Kansai University, 3-3-35 Yamate-cho, Suita 564-8680, Japan

[2]Department of Applied Chemistry, Graduate School of Engineering, The University of Tokyo, Bunkyo-ku, Tokyo 113-8654, Japan

[3]Department of Advanced Materials Science, Graduate School of Frontier Sciences, The University of Tokyo, 5-1-5 Kashiwanoha, Kashiwa, Chiba 277-8561, Japan

[4]The Institute for Solid State Physics, The University of Tokyo, 5-1-5 Kashiwanoha, Kashiwa, Chiba 277-8581, Japan

[5]National Institute of Advanced Industrial Science and Technology (AIST), 1-1-1, Umezono, Tsukuba, Ibaraki 305-8568, Japan

*Correspondence: y.yasuda@kansai-u.ac.jp (Y. Yasuda), kmayumi@issp.u-tokyo.ac.jp (K. Mayumi), kohzo@edu.k.u-tokyo.ac.jp (K. Ito)

Abstract

Slide-ring (SR) gels are a class of polymer gels known for their unique softness, toughness, and high extensibility. The defining structural feature of SR gels is their figure-of-eight-shaped slidable cross-links, whose sliding dynamics are believed to underpin their mechanical properties. However, the relationship between the sliding mechanics and observed mechanical behavior of SR gels remains unclear because their structure differs considerably from those of conventional fixed cross-link gels and vulcanized rubbers. In this work, we employed coarse-grained molecular dynamics simulations to investigate the mechanical behavior of SR gels up to large deformation. By visualizing the correlated distribution of network strand orientation and stress loading, we found that SR gels under strain exhibit uniform chain orientation and efficient stress dispersion throughout the network, in contrast to gels with fixed cross-links, which display regions of highly oriented and heavily stressed chains. Furthermore, we observed that the distribution of network-strand length changes under deformation, indicating that chains are reconfigured into shorter and longer sections during stretching. Notably, we demonstrated that the finite network-strand length (N_{max}) determines the finite extensibility of SR gels, corresponding to the maximum elongation ratio (λ_{max}). These findings provide new insights into the molecular mechanisms driving the high

extensibility and toughness of SR gels and offer valuable guidance for designing SR gels with tailored mechanical properties.

1. Introduction

Hydrogels are cross-linked polymer networks swollen with water, which are widely used as biocompatible materials such as soft contact lens[1,2] and artificial vitreous substitutes.[3] However, the low mechanical toughness of conventional hydrogels limits their use in certain applications. This weakness arises primarily from their inhomogeneous network structure[4] compared with that of other materials such as metals and ceramics and sparse structure compared with that of other polymeric materials including rubbers and plastics. Strands in gel networks have a wide distribution of lengths between cross-links. When stretched, stress concentrates on short polymer strands, which results in brittle fracture.[4,5]

Several tough gels have been developed that address this situation. Gong et al.[6] fabricated a double-network gel composed of a rigid polymer network interpenetrated with a flexible one. This gel achieved both high Young's modulus (~MPa) and fracture energy (~kJ/m^2). Under deformation, the rigid polymer network sacrificially fractured to preserve the flexible network. This toughening mechanism is called the sacrificial bond mechanism,[6,7] which has been applied to various types of tough polymer gels with breakable weak bonds.[8–13]

Another strategy for toughening hydrogels is to form a homogeneous network structure.[14–19] Sakai and colleagues developed quasi-homogeneous hydrogels with uniform network-strand length through cross-linking of tetra-/tri-armed end-functionalized polyethylene glycol (PEG) macromers.[16,17] The quasi-homogeneous structure of these tetra-PEG/tri-PEG gels was confirmed by neutron and light scattering measurements.[19–21] A further example of homogeneous hydrogels are the slide-ring (SR) gels developed by Okumura and Ito[22–24]. SR gels

are fabricated by cross-linking two ring-shaped cyclodextrin (CD) molecules in polyrotaxanes,[25,26] in which many CD rings are threaded on a long PEG chain (Fig. 1(a)). SR gels have high toughness,[24,27–31] which should originate from their unique cross-linking manner of slidable figure-of-eight cross-links.[22,24,32] The figure-of-eight-shaped cross-linking molecules each composed of two CDs can slide along the PEG chains[33] and are believed to act as pulleys to homogenize chain tension under deformation.[32]

To validate this hypothesis, the structures and dynamics of deformed SR gels have been studied by the small-angle neutron and X-ray scattering (SANS and SAXS) techniques.[34,35] SAXS experiments demonstrated that SR gels under uniaxial deformation exhibited less anisotropic patterns than those of conventional gels with fixed cross-linking (hereafter denoted as FC gels), indicating that the sliding of the cross-links suppressed local network deformation.[35] These results indicated the unique local structure change of SR gels under deformation, but direct observation of the underlying molecular mechanisms, especially the sliding mechanism of cross-links, has not yet been achieved.

The local structure changes of SR gels under deformation should contribute to their unique mechanical properties of low Young's modulus,[27,32,36,37], strain-softening behavior[28,29,37], high stretchability,[24,27,28] and fracture resistance.[27,29] Sliding mechanics under deformation also drive the phase separation of rings and chains in low-coverage (2%) polyrotaxanes, which enables strain-induced crystallization and further increases toughness.[30,31] Although the mechanical properties of SR are closely related to their local structural changes, the detailed molecular mechanisms have not been cleared experimentally. The structure–property relationship between the sliding of cross-links and mechanical properties of SR gels has been studied by coarse-grained molecular dynamics (MD) simulations[38–42]. Koga and Tanaka conducted pioneering MD simulations of tri--branched rubbers with mobile cross-links[38]. Gavrilov and Potemkin constructed a coarse-grained model of SR gels using the bead–spring model for both figure-of-eight cross-links and polymer chains, reproducing the softness, uniaxial stretchability, and

permeability of SR gels.[39] Uehara et al. simulated the fracture behavior of SR gels; they found that SR gels become highly oriented along the stretching direction under uniaxial deformation and fracture occurs from the terminal bond of the polyrotaxanes.[42] Chen, Rubinstein and co-workers have successfully established a theoretical model explaining the strain-softening behavior observed in their[37] and our[40] simulation results and experimental[28] result, based on classical entanglement theory.[37] However, these previous works do not give us a quantitative relationship between the sliding motion of the cross-links and mechanical properties of SR gels.

In our previous work, we constructed coarse-grained models of polyrotaxanes[43] and SR gels[40] and performed MD simulations of SR gels to realize mechanical analysis focusing on the slight deformation region. We found that the network-strand length distribution changed from a random distribution in the unstretched state to a bimodal distribution under stretching. This suggests that the sliding of the cross-links causes the network strands to segregate into longer ones oriented along the stretching direction and shorter ones, which lowers chain tension and the macroscopic stress of stretched SR networks. From the partial network-strand length distributions, we evaluated the sliding degree of the cross-links, N_{slide}, and modified the three-chain model[44,45] to connect N_{slide} with the low Young's modulus of SR gels for three inclusion ratios (IRs). IR is defined as the fraction of ring molecules to beads in the chain. The modified three-chain model can be expressed as,[40]

$$E_{\mathrm{SR}} = E_{\mathrm{affine}}\left(1 - \frac{N_{\mathrm{slide}}}{N_0}\right)^2. \quad (1)$$

where E_{SR} is the Young's moduli of SR gels, E_{affine} is theoretical estimation by the affine network model[44], and N_0 is the average bead number of network-strands. Our prior work focused on SR networks at relatively low strain and explaining their low Young's modulus.

This study extends the investigation to large uniaxial deformations. Through MD simulations, we examine the network structure and stress distribution of SR gels across a wide strain range. We also conducted network-strand length analysis under deformation, and using the obtained parameters N_{slide} and N_{max}, we succeeded in constructing quantitative model reproducing

Young's moduli and finite extensibility using the parameters related to the parameters. This work provides deeper insights into the molecular mechanisms underlying stress homogenization and the soft mechanical response of SR gels, suggesting a way to design materials with tailored mechanical properties.

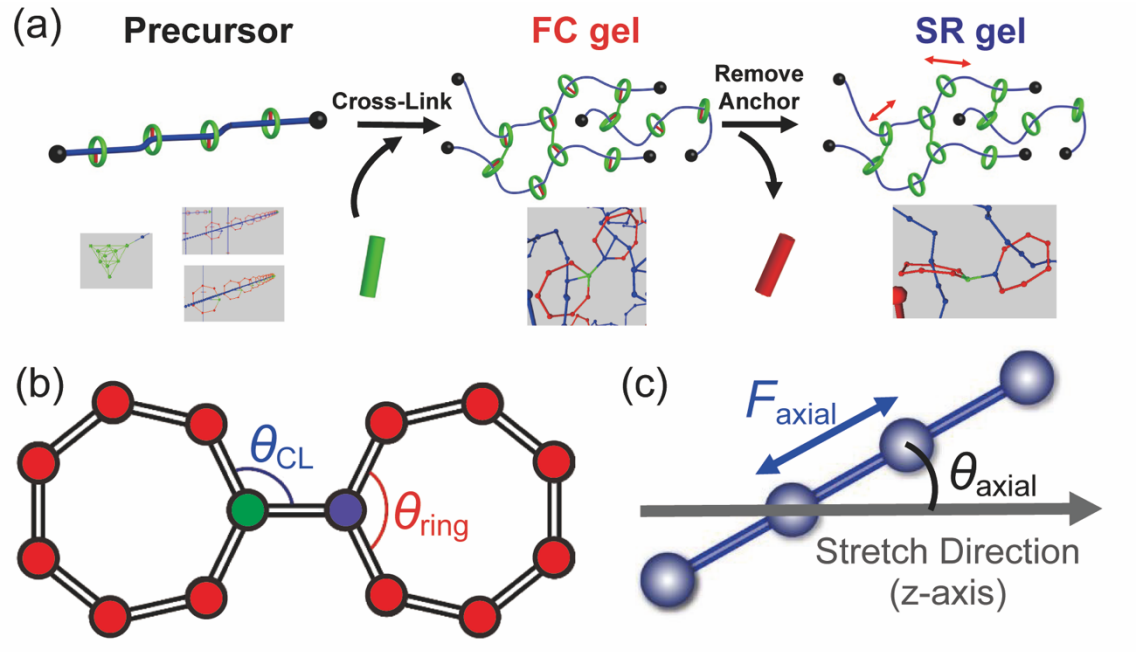

Fig. 1 Schematic illustrations of the simulated systems and analysis: (a) fabrication process of FC and SR gels, (b) coarse-grained model of a figure-of-eight cross-link and the definition of θ_{CL} and θ_{ring}, and (c) axial bond force F_{axial} and orientation angle θ_{axial} of an axial polymer strand under elongation.

2. Method

2.1 Coarse-grained model of SR and FC gels

Following our previous work,[40] we used a coarse-grained spring–bead model for SR gels. SR gels were derived from FC gels by converting fixed cross-linking points into slidable ones, enabling a direct comparison between FC and SR gels with identical network structure (Fig.

1(a)). To construct the models, we prepared precursors with rings threaded onto linear polymer chains that were capped at both ends by bulky tetrahedral units. The rings were anchored to the linear chains at regular intervals, as shown in Fig. 1(a). Seven-membered rings were used because they can slide freely along the coarse-grained polymer chain[43] (Fig. 1(b)). Each axial chain consisted of 400 beads. The number of rings on each chain was 8, 12, 20, 28, or 40, corresponding to an IR of 2%, 3%, 5%, 7%, or 10%, respectively. We generated 200 precursors in a simulation box with sides of 100σ, achieving a number density φ of 0.08 [σ^{-3}], where σ is the unit of length in the simulation.

The system was first relaxed for $10^6\tau$, where τ is the unit of time in the simulation. Subsequently, a cross-linking reaction was simulated for $10^5\tau$ to generate FC gels by binding two anchoring beads (green and blue beads in Fig. 1(b)) on different rings. Two anchoring beads were connected by a cross-link (shown as a green bond in Fig. 1(a)) if they approached within a distance of 1.3σ, following the approach in previous work on cross-linked rubbers[46]. A-type and B-type precursors with different anchoring beads, A and B, respectively, were generated in the same number. Self-crosslinking was prevented by allowing only A-B reactions. In this way, we obtained the structure of FC gels.

The FC gels were then converted into SR gels by removing the anchor bonds (red bonds in Fig. 1(a)) between the rings on the chains so that the rings were able to slide. Samples are named according to their IR. The binding ratio (r_B) and cross-linking density (ν_C) of samples with different IRs are summarized in Table 1. In total, ten systems were investigated (FC gels with five IRs and their corresponding SR gels). The binding ratio was over 84% for all the gels, resulting in ν_C of 0.71–3.38×$10^{-3}\sigma^{-3}$. Before elongation of the FC and SR gels, we conducted a relaxation calculation for $10^5\tau$. For uniaxial elongation calculations, the volume of the gels was kept constant (Poisson ratio = 0.5), the elongation speed was set to 10^{-3} [σ/τ] (equivalent to 100% / 10^5 τ), and the data output interval was $2\times10^3\tau$. The deformation speed dependence on the stress-elongation ratio curves and Young's moduli are present in the Fig. S1 in the Supporting Information. The

elongation simulations were terminated when any bond length accidentally exceeded 1.5σ. Equilibrium calculations were performed for $1\times10^4\tau$ with data outputs recorded every $1\times10^2\tau$ (yielding 100 snapshots). The initial structure for each equilibrium calculation was obtained at every 50% deformation increment (i.e. $\Delta\lambda$ = 0.5 in the elongation ratio λ). These equilibrium snapshots were used for orientation index distribution, axial bond force distribution, and network strand length distribution analyses. From snapshots taken at λ =1,2,3,4 and 5, we also evaluated the stress-relaxation properties of the SR gels, which exhibit almost no stress relaxation, as illustrated in Fig. S2 in the Supporting Information.

Table 1 Parameters of samples with different IRs

Sample	IR 2%	IR 3%	IR 5%	IR 7%	IR 10%
Inclusion ratio (IR) [%]	2	3	5	7	10
Binding ratio (r_B) [%]	88.1	89.3	89.4	87.0	84.0
Cross-linking density (ν_C) [$10^{-3}\sigma^{-3}$]	0.71	1.07	1.79	2.44	3.38

2.2 Bonding and non-bonding interactions and thermostat

The simulations employed the Kremer–Grest bead–spring model for both FC and SR gels. The bonding and non-bonding potentials, $U_{\mathrm{bond}}(r)$ and $U_{\mathrm{nonbond}}(r)$, respectively, were defined as:

$$U_{\mathrm{bond}}(r) = U_{\mathrm{FENE}} + U_{\mathrm{WCA}}, \tag{2}$$

$$U_{\mathrm{nonbond}}(r) = U_{\mathrm{WCA}}. \tag{3}$$

Here,

$$U_{\mathrm{FENE}}(r) = \begin{cases} -15\varepsilon\left(\frac{R_0}{\sigma}\right)^2 \ln\left[1-\left(\frac{r}{R_0}\right)^2\right], & r < R_0 \\ \infty, & r \geq R_0 \end{cases}, \tag{4}$$

$$U_{\mathrm{WCA}}(r) = \begin{cases} 4\varepsilon\left[\left\{\left(\frac{\sigma}{r}\right)^{12} - \left(\frac{\sigma}{r}\right)^{6}\right\} - \frac{1}{4}\right], & r < 2^{\frac{1}{6}} \\ 0, & r \geq 2^{\frac{1}{6}} \end{cases}. \tag{5}$$

$U_{FENE}(r)$ and $U_{WCA}(r)$ are the finite extensible-nonlinear spring (FENE) potential and purely repulsive Weeks–Chandler–Anderson interactions, respectively. ε is the unit of energy, where $\tau = \sigma\sqrt{(m/\varepsilon)}$ and m is the mass of all beads. R_0 is the maximum bond length, and it is set to a constant value of 1.5 σ . To keep the rings rigid, we introduced two types of angle potentials for the inner and outer angles of the rings:

$$U_{\text{angle}}(\theta_{\text{ring}}) = 50\,\varepsilon\left(\theta_{\text{ring}} - \frac{5\pi}{7}\right)^2, \qquad U_{\text{angle}}(\theta_{\text{CL}}) = 50\,\varepsilon\left(\theta_{\text{CL}} - \frac{9\pi}{14}\right)^2. \tag{6}$$

The dynamics of each bead were set to follow Langevin dynamics with friction $\Gamma = 0.5\tau^{-1}$ and temperature T = 1.0 ε/k_B, where k_B is the Boltzmann constant. To decrease the total number of beads in the systems, solvent was not introduced explicitly but expressed as a random force in the Langevin equation. The time step was $\Delta t = 0.01\tau$. Simulations were performed using OCTA8/COGNAC92[47] and modified LAMMPS.[48]

2.3 Analysis

2.3.1. Partial chain length distribution

The network-strand lengths between slidable cross-links were calculated following the method described in our previous work.[43] One-dimensional coordinate indices were defined along the axial chain from one polymer end to the other (1 to 400). The position of a ring in a sliding cross-link was defined by the coordinate index of the chain bead nearest to the ring in the same manner as in our previous work[43]. The number of beads in the network strands between neighboring cross-links, $N_{partial}$, was calculated using the difference between the indices of adjacent rings.

2.3.2. Stress calculation

The stress tensor **σ** was calculated using the following virial:

$$\boldsymbol{\sigma} = \frac{1}{\mathrm{V}}\left\{\langle\sum_{\mathrm{i}=1}^{\mathrm{i}\in\mathrm{V}} m_{\mathrm{i}}\boldsymbol{v}_{\mathrm{i}} \otimes \boldsymbol{v}_{\mathrm{i}}\rangle + \frac{1}{2}\langle\sum_{\mathrm{i}}^{\mathrm{i}\in\mathrm{V}}\sum_{\mathrm{j}\neq\mathrm{i}}^{\mathrm{j}\in\mathrm{V}} \boldsymbol{r}_{\mathrm{ij}} \otimes \boldsymbol{F}_{\mathrm{ij}}\rangle\right\}. \quad (7)$$

Here, <> denotes a time average, V represents the simulation cell with volume = $1.0\times10^6\sigma^3$, m_{i} = 1 m is the mass of bead *i*, $\boldsymbol{v}_{\mathrm{i}}$ is the velocity of bead *i*, $\boldsymbol{r}_{\mathrm{ij}}$ is the relative position from bead *i* to bead *j*, and $\boldsymbol{F}_{\mathrm{ij}}$ is the force exerted by bead *i* on bead *j*, which is given by the differentiation of Eq. 2 and 3. The true stress, σ_{true}, was determined using the diagonal components σ_{xx}, σ_{yy}, and σ_{zz}:

$$\sigma_{\mathrm{true}} = \sigma_{\mathrm{zz}} - \frac{\sigma_{\mathrm{xx}}+\sigma_{\mathrm{yy}}}{2}. \quad (8)$$

σ_{true} was converted into engineering stress σ_{eng} using the following equation,

$$\sigma_{\mathrm{eng}} = \frac{\sigma_{\mathrm{true}}}{\lambda} \quad . \quad (9)$$

The main results are discussed for elongation along z-direction. To assess the uncertainty of our simulations, we also conducted elongation simulations along the x and y direction. Additionally, we fabricated another configuration for all IRs. The magnitudes of the initial structures, as reflected in the stress-elongation ratio curves, are shown in Fig. S3 in the Supporting Information, indicating that only a slight dependence on system size.

2.3.3. Orientation and force of axial chains

To evaluate the orientation of the axial chains, first- and second-order nematic order parameters were defined as follows. The direction of each bond in the axial chains was represented by the bond vector $\boldsymbol{r}_{\mathrm{axial}}$, which is referred to as the axial vector hereafter. θ_{axial} was defined as the angle between $\boldsymbol{r}_{\mathrm{axial}}$ and the elongation direction $\boldsymbol{r}_{\mathrm{z}}$ = [0,0,1] (Fig. 1(c)).

The bond orientation was quantified using two parameters, orientation index ($|\cos\theta_{\mathrm{axial}}|$) and P_2. The former was determined using the following equation,

$$|\cos\theta_{\mathrm{axial}}| = \frac{|\mathbf{r}_{\mathrm{axial}}\cdot\mathbf{r}_{\mathrm{z}}|}{|\mathbf{r}_{\mathrm{axial}}|} \quad , \quad (10)$$

where a value of 1 indicates alignment parallel to the elongation direction. $|\cos\theta| = 0$ represents a direction perpendicular to the elongation direction. We employed this orientation index to analyze the distribution of chain orientation because it shows a uniform distribution when $\boldsymbol{r}_{\mathrm{axial}}$ is

isotropically distributed.

The instantaneous and averaged order parameters p_2 and P_2 was calculated using the following equation,

$$p_2 = \frac{3\cos^2\theta_{\text{axial}}-1}{2}, P_2 = \langle p_2 \rangle. \quad (11)$$

We employed P_2 to analyze average orientation because it equals zero when $\boldsymbol{r}_{\text{axial}}$ is isotropically distributed. P_2 ranges from −0.5 to 1, where 1 indicates complete alignment parallel to the elongation direction.

The force acting on each bond of the axial chains, F_{axial}, was calculated as a function of the bond vector $\boldsymbol{r}_{\text{axial}}$:

$$F_{\text{axial}}(|\boldsymbol{r}_{\text{axial}}|) = -\frac{\partial U_{\text{bond}}(r)}{\partial r}\Big|_{r=|\boldsymbol{r}_{\text{axial}}|}. \quad (12)$$

3. Results and Discussion

3.1. Mechanical properties of fixed-cross-link and slide-ring gels

Stress–elongation ratio curves

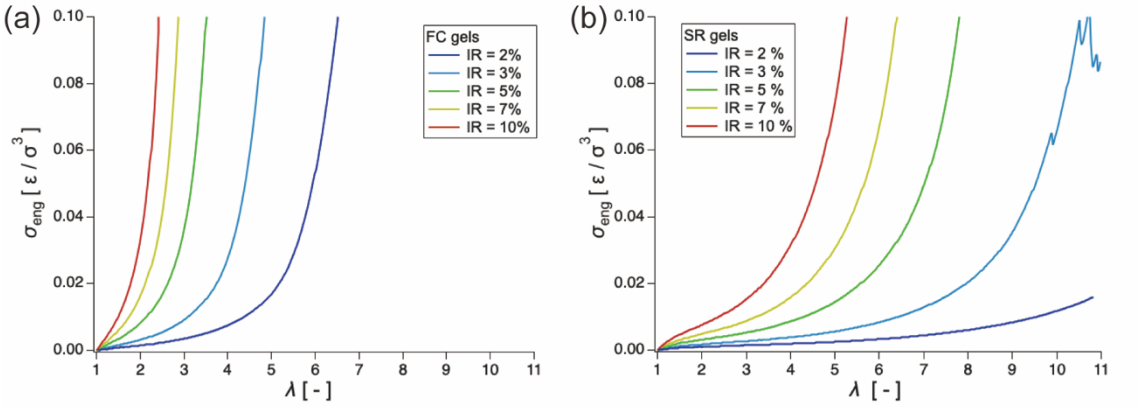

Fig. 2 Stress (σ_{eng})–extension ratio (λ) curves of (a) FC and (b) SR gels with different IRs.

Figure 2(a) and (b) present the simulated stress–elongation ratio (σ_{eng}–λ) curves of the SR and FC gels with various IRs. The SR gels exhibit smaller stresses than the corresponding FC gels, reflecting the relative softness of SR gels, which is consistent with experimental

observations.[27,32,36] As demonstrated in our previous work, the lower elasticity of SR gels compared with that of FC gels is attributed to the sliding behavior of the cross-links.[40] In the high strain range, the σ_{eng}–λ curves exhibit strain-hardening behavior, which is caused by the finite extensibility of the polymer chains[45]. When comparing the two types of gels with the same IR, the SR gels show delayed strain hardening compared with the FC gels, which corresponds to the higher extensibility[24,27,28] of SR gels than FC gels. An experimental stress–elongation ratio curve[29] is also shown in Fig. S4 in the Supporting Information. for comparison; this experimental curve agrees with our simulated ones. This validation confirms that the coarse-grained model is qualitatively realistic, allowing reliable structural analysis.

Axial chain orientation

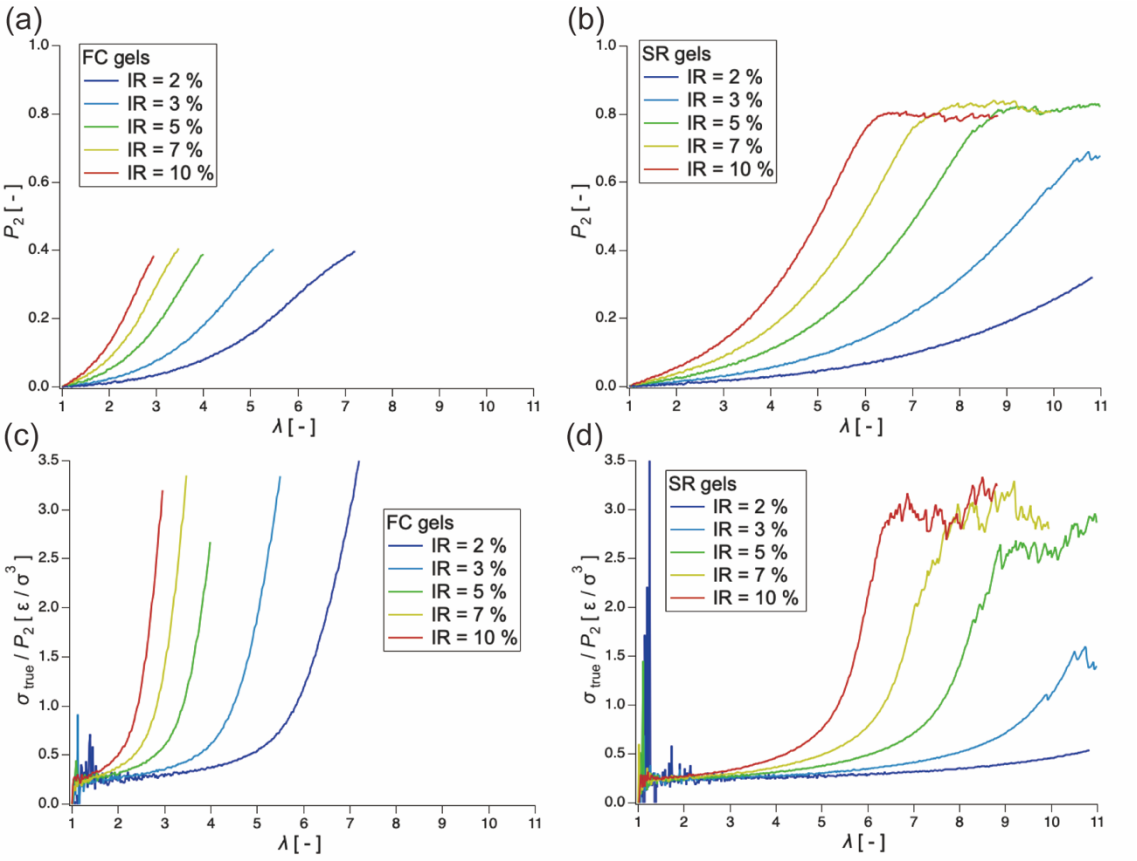

Fig. 3 Order parameter P_2 for (a) FC and (b) SR gels. $\sigma_{\mathrm{true}}/P_2$ for (c) FC and (d) SR gels.

In the small deformation regime, stress in elastomers originates from the loss of conformational entropy in network strands driven by chain orientation[45], a phenomenon referred to as the "entropy elasticity" of rubbers. In this regime, the true stress σ_{true} is proportional to P_2 of the chains, which is known as the "law of photoelasticity" [49,50]. Figure 3(a) and (b) present the dependence of P_2 on elongation ratio λ for axial polymer chains in FC and SR gels. For SR and FC gels with the same IR, P_2 is smaller in SR gels, indicating that chain deformation is more relaxed than in FC gels. Figure 3(c) and (d) plot σ_{true}/P_2 against λ to examine photoelasticity. At low strain, σ_{true}/P_2 remains constant, confirming that stress in this regime is driven by entropy elasticity. Interestingly, the constant is around 0.25 independent of IR and gel type, implying that the softness of SR gels originates from the low orientation of polymer chains. At larger deformation, σ_{true}/P_2 begins to increase, implying that the elasticity becomes non-entropic. This upturn of σ_{true}/P_2 is delayed in SR gels compared with that of FC gels, indicating that the entropic elasticity regime is broader in SR gels than in FC ones.

Average force loaded on axial chains

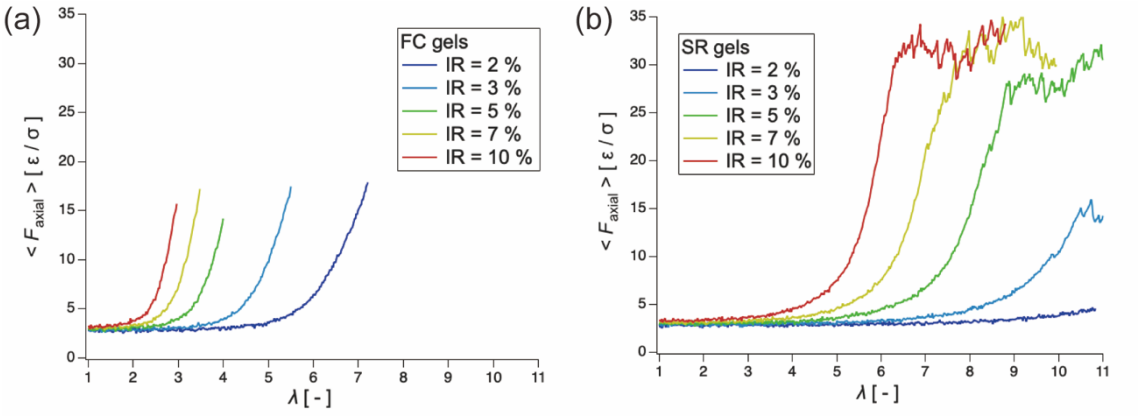

Fig. 4 Average force loaded on axial chains $<F_{axial}>$ for (a) FC and (b) SR gels.

To observe energy elasticity directly, the average force loaded on axial bonds, $\langle F_{axial} \rangle$, was analyzed and is plotted against λ in Figure 4(a) and (b) for FC and SR gels, respectively. Like

σ_{true}/P_2, $\langle F_{axial} \rangle$ is constant at small elongation, but rises sharply as deformation increases. This behavior confirms that the upturn of σ_{true}/P_2 is driven by energy elasticity resulting from stress concentration on axial chains, whereas elasticity in the small deformation regime originates from entropic elasticity caused by polymer chain orientation. The analysis also reveals that sliding cross-links extend the entropy elasticity region, especially for gels with low IR. SR gels exhibited higher maximum P_2 and $\langle F_{axial} \rangle$ than corresponding FC gels, suggesting that the stress dispersion mechanism involves the formation of a highly ordered and stress-dispersed structure. To further explore this molecular insight, we investigated the distributions of chain orientations and forces loaded on axial chains, which will be discussed in Section 3.2.

3.2. Local stress and strain distribution

Stress and strain concentration in FC gels

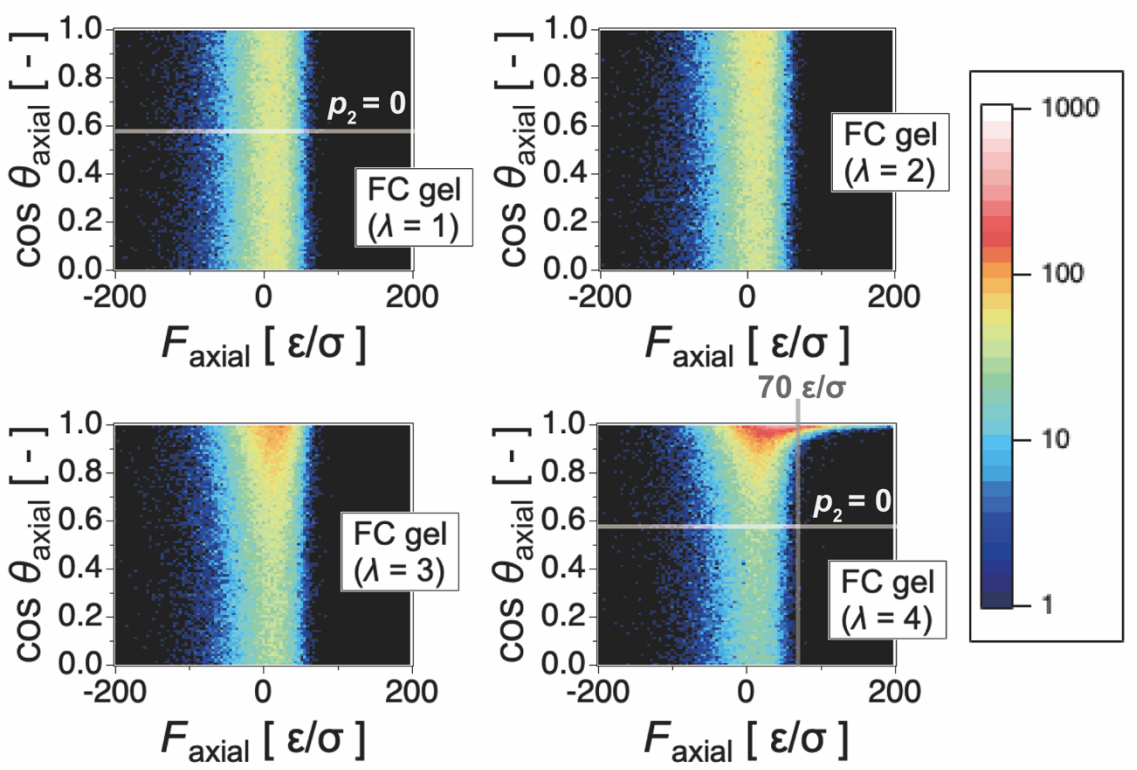

Fig. 5 Distribution of force loaded on axial chains F_{axial} and bond orientation $|\cos\theta|$ for FC gels (IR = 5%).

To investigate the origin of the distinctive softness and toughness of SR gels compared with the properties of conventional FC gels, we analyzed the distribution of local stress and strain by visualizing the distributions of loaded on axial chains (F_{axial}) and bond orientation indices ($|\cos \theta_{\mathrm{axial}}|$) in stretched gels. Fig. 5(a–d) show two-dimensional heatmaps of these distributions for the FC gel with IR = 5%. In the undeformed state ($\lambda = 1$, Fig. 5(a)), there is no bias in the vertical axis, showing that axial bonds are isotropically distributed. F_{axial} are symmetrically distributed around zero because of thermal fluctuations. The ratio of chains oriented in the stretching direction ($p_2(\theta_{\mathrm{axial}}) > 0$) was calculated to be 42.1%, which is close to 42.3%, the theoretical value in the case of an isotropic distribution.

At $\lambda = 3$, some chain bonds become highly oriented in the stretching direction ($|\cos \theta_{\mathrm{axial}}| \sim 1$), as shown in Fig. 5(c), which drives the increase of $\langle F_{\mathrm{axial}} \rangle$ observed in Fig. 4(a). By $\lambda = 5$, $\langle F_{\mathrm{axial}} \rangle$ only increases further on highly ordered chains; most chains remain randomly oriented and unstressed. This reveals inhomogeneous stress concentration in FC gels during elongation. The ratio of chains oriented in the stretching direction increases to 71.3% at $\lambda = 4$, which is a 29.2% increase from that of the undeformed state.

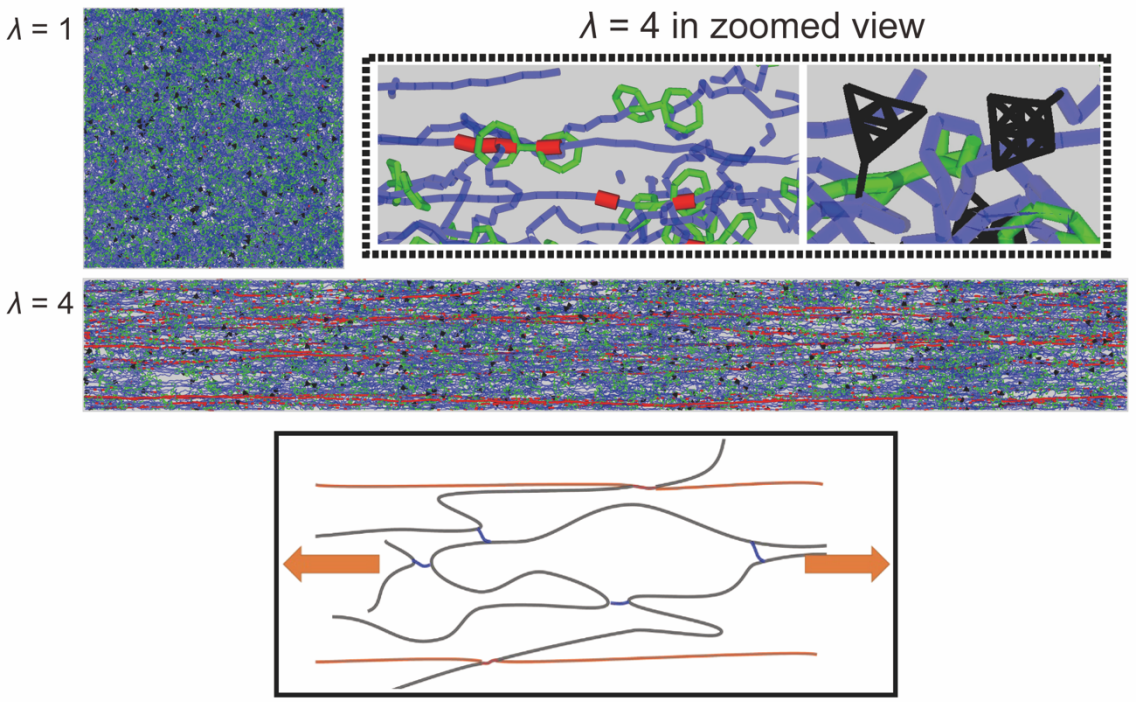

Fig. 6 Snapshots of an FC gel (IR = 5%) at λ = 1 and 8. Anchored rings and figure-of-eight cross-links are drawn in green; the main chain is colored in blue, and the end-capping groups are represented as black rods (as shown in the zoomed view). Stress-concentrated bonds are highlighted in red. A schematic illustration of the deformation mechanisms of FC gels under uniaxial stretching are also shown.

Figure 6 presents snapshots of the FC gel with IR = 5% at various elongation ratios. Stress-loaded chains with $F_{axial} > 70\ \varepsilon/\sigma$ are highlighted in red. At λ = 4, these stress-concentrated bonds form linear percolated structures aligned with the stretching direction. The inset schematic in Fig. 6 illustrates that during elongation, a small fraction of polymer chains in FC gels bears most of the applied stress, while the majority of chains remain unstressed and fluctuate freely. This inhomogeneous stress distribution leads to the brittle fracture behavior observed for FC gels.

Stress and strain homogenization in SR gels

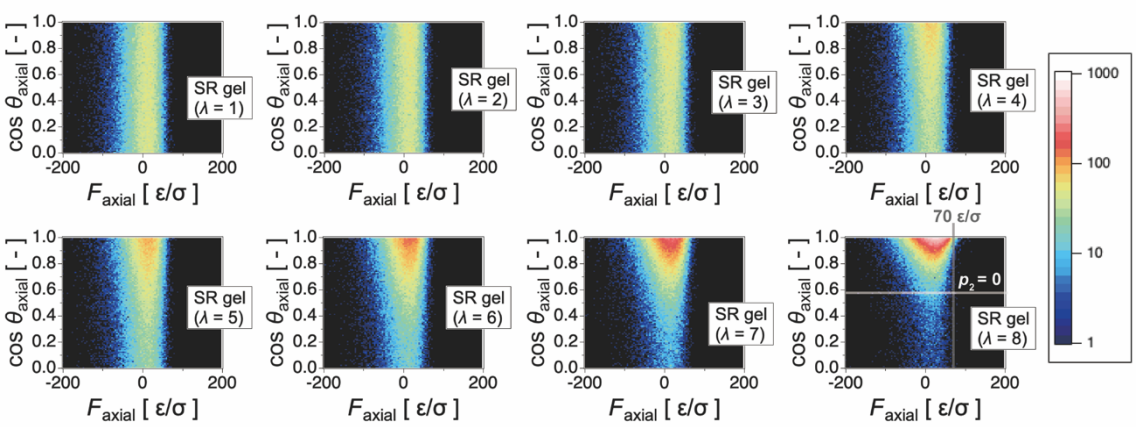

Fig. 7 Distribution of force loaded on axial chains F_{axial} and bond orientation index $|\cos \theta_{axial}|$ for SR gels (IR = 5%).

In contrast to the case for FC gels, polymer chains in SR gels deform more homogeneously. In the undeformed state (λ = 1, Fig. 5(a)), there is no bias in the vertical axis, showing that axial bonds are isotropically distributed. F_{axial} is symmetrically distributed around zero because of thermal fluctuations. The ratio of chains oriented in the stretching direction ($p_2(\theta_{axial}) > 0$) was also calculated to be 42.1%, the same as that of the FC gels.

For SR gels with IR = 5%, the F_{axial} distribution becomes biased toward an oriented state ($|\cos \theta_{axial}| \sim 1$) as λ increases. However, the fraction of oriented chains in each SR gel is smaller than that in the corresponding FC gel at the same λ, indicating that the sliding of cross-links lowers internal strain on chains. At λ = 8, nearly all chains (93.9%) are oriented in the stretching direction, representing an increase of 51.8% from that of the undeformed state. This uniform chain orientation contributes to high average order parameters and strain homogenization across the network strands.

When comparing an FC gel at λ = 4 and corresponding SR gel at λ = 8 (these gels had similar $\langle F_{axial} \rangle$ values of 14.18 ε/σ and 14.39 ε/σ, respectively), F_{axial}s in the SR gel are more evenly distributed and exhibit smaller variance than those in the FC gel. This indicates that stresses are homogenously distributed in SR gels. Fig. S6 in the Supporting Information shows

P_2 of and forces loaded on the cross-linking bond and chain-end groups of FC and SR gels in addition to axial chains. The results indicate that all bond types in SR gels align with the stretching direction and experience stress at finite elongation, whereas in FC gels, only axial and cross-linking bonds exhibit such behavior.

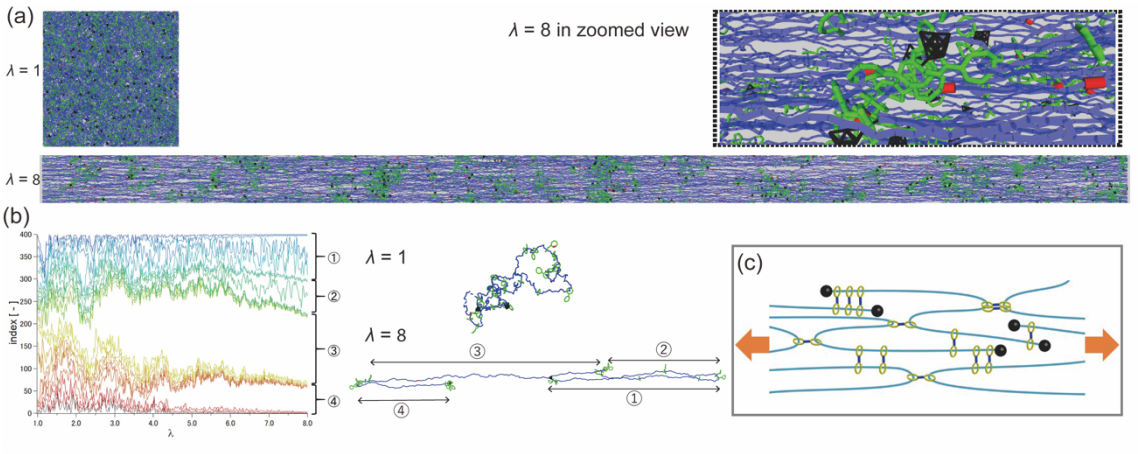

Fig. 8 (a) Snapshots of an SR gel (IR=5%) at λ = 1 and 8. Rings and figure-of-eight cross-links are drawn in green; the main chain is colored in blue, and the end-capping groups are represented as black rods (as shown in the zoomed view). Stress-concentrated bonds are highlighted in red. (b) Position index of the slide-ring cross-links on an axial chain in SR gel (IR = 5%) at various extension ratios and snapshots of the SR network at λ = 1 and 8. (c) A schematic illustration of an SR gel under uniaxial stretching.

Molecular mechanism of stress homogenization by sliding cross-links

The stress homogenization was further confirmed by snapshots of the SR gel at λ = 8 (Fig. 8(b)). Unlike the extended FC gel, stress-concentrated red bonds were dispersed randomly throughout the SR network rather than forming percolated structures. A magnified snapshot of the SR gel at λ=8 reveals that most slide-ring cross-links are aggregated, and network strands are extracted and align to stretching direction.

To further understand the sliding behavior, the one-dimensional coordinate of slide-ring

cross-links along a chain at various stretching degrees was determined. Fig. 8(b) shows the coordinate of the rings and slide-ring cross-links on one polyrotaxane axial chain in an SR gel plotted against λ and snapshots of the polyrotaxane in undeformed (λ = 1) and stretched (λ = 8) states. As shown in the graph, rings and slide-ring cross-links are randomly distributed in undeformed state, whereas some slide-ring cross-links aggregate near the chain ends or become stuck at chain kinks in the stretched state (λ=8). This behavior is consistent with the results of Uehera et al.[42], in which it is insisted that fracture of SR gels begins from the end groups of polyrotaxanes. Fig. 8(c) presents an illustration of the network structure in highly stretched SR gels. The sliding and aggregation of cross-links allow stress redistribution, preventing the formation of stress-concentrated regions. This mechanism enhances the toughness and stretchability of SR gels, providing a clear contrast to the brittle fracture behavior of FC gels.

3.3. Quantitative structure–mechanical property relationship of SR gels

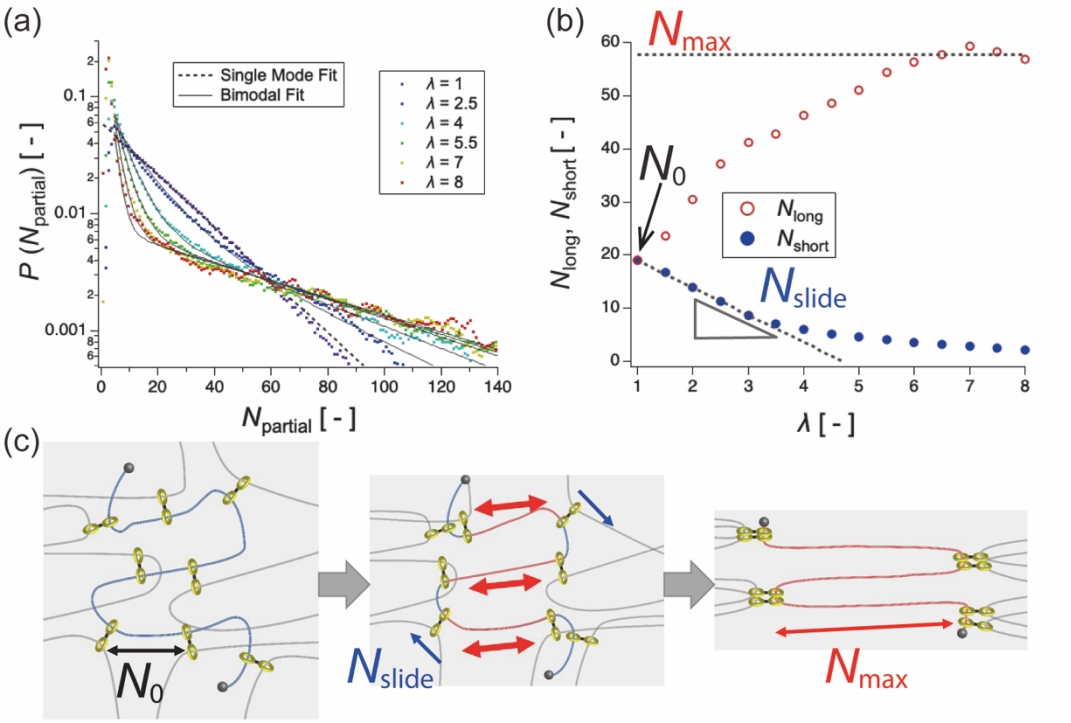

Fig. 9 (a) Distribution of $N_{partial}$ for an SR gel with IR = 5%. The dotted line is the single-exponential fitting result (Eq. 13) for $\lambda = 1$, and the solid lines are the fitting lines using the bimodal function (Eq. 15). (b) Dependence of N_{short} and N_{long} on λ for the SR gel with IR = 5%. (c) Schematic illustrations of N_0, N^0_{slide}, and N_{max}.

Table 2 N_0^{exp}, N_0, N^0_{slide}, and N_{max} of SR gels with different IRs

IR	2%	3%	5%	7%	10%
N_0^{exp}	56.8	37.3	22.4	16.4	11.9
N_0	50.0	32.8	18.9	13.5	9.26
N^0_{slide}	9.47	7.53	4.86	3.73	2.62
N_{max}	142	107	57.6	39.5	30.9

Partial chain distribution driven by sliding

To further elucidate the unique mechanical behavior of SR gels, we analyzed the sliding behavior of cross-links in stretched SR gels by evaluating the length distribution of network strands between cross-links. Fig. 9(a) shows the distribution of N_{partial} for an SR gel with IR = 5% in the undeformed state (λ = 1). In this state, the slide-ring cross-links are randomly distributed along the polymer chains, and the distribution function $P(N_{\mathrm{partial}})$ follows an exponential distribution:

$$P\left(N_{\mathrm{partial}}\right) \approx \frac{1}{N_0}\exp\left(-\frac{N_{\mathrm{partial}}}{N_0}\right), \tag{13}$$

where N_0 is the average bead number of network strands. By fitting $P(N_{\mathrm{partial}})$ for $\lambda = 1$ with eq. 13, we obtained N_0 values for the SR gels with different IRs, as listed in Table 2. The estimated N_0 values are close to the average network-strand length N_0^{exp} expected from the IR and r_{B}, indicating that SR cross-links are one-dimensionally distributed with a Poisson distribution:

$$N_0^{\mathrm{exp}} = \frac{1}{\frac{IR\,[\%]}{100}\times r_{\mathrm{B}}}. \tag{14}$$

Under stretching, $P(N_{\mathrm{partial}})$ changes to bimodal, as shown in Fig. 9(a) and also in previous studies.[38–40] The difference between slopes in the first and second modes gets larger and gradually converges to a specific distribution at large deformation (about λ > 5.5). This mode split is consistent with the observation that the sliding of the cross-links under stretching results in the split of the network strands into a bimodal distribution of longer strands and shorter strands, as illustrated in Fig. 8. It is also proved that both longer and shorter groups of strands show exponential distributions, which can be described as:

$$P(N_{\mathrm{partial}},\lambda) = \frac{A_{\mathrm{short}}}{N_{\mathrm{short}}(\lambda)}\exp\left(-\frac{N_{\mathrm{partial}}}{N_{\mathrm{short}}(\lambda)}\right) + \frac{A_{\mathrm{long}}}{N_{\mathrm{long}}(\lambda)}\exp\left(-\frac{N_{\mathrm{partial}}}{N_{\mathrm{long}}(\lambda)}\right). \tag{15}$$

The partial chain distribution was fitted by the model function (Eq. 15) to obtain the plot in Fig. 9(b). N_{short} and N_{long} correspond to average bead numbers in the long and short network strands, respectively, as illustrated in Fig. 9(c). As shown in Fig. 9(b), with the increase of λ, N_{short}

decreases to zero, whereas N_{long} increases and saturates at a maximum value, N_{max}. At the high λ where N_{short} and N_{long} reach saturated values, the slide-ring cross-links are stuck at the ends or kinks of the polymer chains, and only the longer polymer strands remain oriented in the elongation direction (Fig. 8(c)).

In our previous work[40], we defined N_{slide} value only in the initial deformation region, treating it as a constant. Here, we rename this constant as N^0_{slide}, which corresponds to the initial slope of the N_{short} with respect to λ:

$$N^0_{\mathrm{slide}} = -\frac{\partial N_{\mathrm{short}}(\lambda)}{\partial \lambda}\Big|_{\lambda=1}. \tag{16}$$

To extend the definition of N_{slide} to various elongation ratios, we propose an extended definition of N_{slide} as a function of λ that represents the average sliding rate during deformation:

$$N_{\mathrm{slide}}(\lambda) \stackrel{\mathrm{def}}{\equiv} \frac{N_0 - N_{\mathrm{short}}(\lambda)}{\lambda - 1}. \tag{17}$$

In the limit λ→1, Eq. 17 becomes Eq. 16. For an analytical expression of N_{short} and N_{slide}, we assume a numerical model curve of N_{short} using the following logistic function:

$$N_{\mathrm{short}}(\lambda) = N_0\left[1 + \tanh\left\{-\frac{N^0_{\mathrm{slide}}}{N_0}(\lambda - 1)\right\}\right] \tag{18}$$

In the Fig. 9(b) and Fig. S7 in the Supporting Information, the fitting curves by Eq. 18 are shown. From these fittings, N^0_{slide} is evaluated and summarized in Table 2. For all IRs, the model curves agree well with the decay curve of $N_{short}(\lambda)$. Substituting Eq. 18 into Eq. 17, $N_{slide}(\lambda)$ yields:

$$N_{\mathrm{slide}}(\lambda) = -\frac{N_0 \tanh\left\{-\frac{N^0_{\mathrm{slide}}}{N_0}(\lambda - 1)\right\}}{\lambda - 1} \tag{19}$$

One can easily show that $N_{slide}(\lambda)$ satisfies Eq. 16 and the following conditions:

$$\begin{cases} N_{\mathrm{slide}}(\lambda) \xrightarrow{\lambda \to 1} N^0_{\mathrm{slide}} \\ N_{\mathrm{slide}}(\lambda) \xrightarrow{\lambda \to \infty} 0 \end{cases} \tag{20}$$

which confirms that the extended definition is consistent with the initial definition and properly

reflects the average sliding behavior over the full range of deformation.

Correlation between sliding parameters and mechanical properties

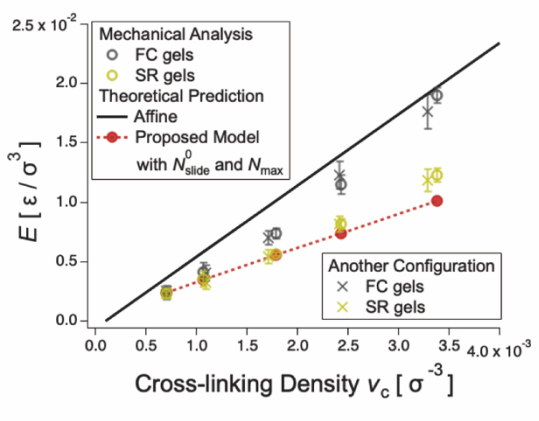

Fig. 10 Dependence of the Young's modulus of FC gels (black symbols) and SR gels (yellow symbols) on cross-linking density. The black solid and red dotted lines are the predictions by the affine network model (Eq. 22) and three-chain model that takes N^0_{slide} into account (Eq. 21).

Values of N^0_{slide} and N_{max} for SR gels with various IRs are summarized in Table 2. Both parameters decrease as IR increases. Notably, N_{max} is approximately three times N_0 for all SR gels. Fig. 9(c) illustrates the network transformation of SR gels. At intermediate strain, cross-links slide along polymer chains by a degree corresponding to $N_{slide}(\lambda)$, generating longer and shorter strands (represented by red and blue strands in Fig. 9(c), respectively). Under finite elongation, shorter strands disappear, leaving longer chains of length N_{max} aligned with the stretching direction, which was also confirmed by the snapshots in Fig. 8.

The relationship between N^0_{slide}, N_{max}, and the mechanical properties of SR gels was investigated using our three-chain model[40], which accounts for the sliding motion of sliding cross-links along network strands. The Young's modulus (E_{SR}) for SR gels is given by:

$$E_{SR} = E_{affine}\left(1 - \frac{N^0_{slide}}{N_0}\right)^2. \quad (21)$$

Here, E_{affine} is the Young's modulus estimated by the affine network model[44]:

$$E_{\mathrm{affine}} = 3\frac{n}{V}k_{\mathrm{B}}T, \tag{22}$$

where n is the total number of network strands, V is the system volume, and T is the temperature. Fig. 10 shows the Young's moduli averaged for three directions, using the configuration illustrated in Table 1, along with the theoretical predictions by Eq. 21 and the corresponding values in Table 2. Additionally, we have included in Fig. 10 the Young's moduli using another configuration explained Section S3 in the Supporting Information. The figure demonstrates that simulated Young's moduli of the SR gels correspond well with the theoretical prediction, even for gels with low IR (2% and 3%), consistent with our previous findings for gels with IR of 5%, 7%, and 10%.

It is also found that Eq. 21 resembles to the theoretical prediction by Edwards-Vilgis model[51,52], under the assumption that all the cross-links are slip-links ($N_c = 0$ in their formulation)

$$G_{\mathrm{slip-link}} = G_{\mathrm{affine}}\frac{1}{(1+\eta)^2}. \tag{23}$$

Where η is defined as measure of slippage in the theory. In the limit $\eta \ll 1$, $1/(1+\eta)$ can be approximated as $1-\eta$. Based on this approximation, Eqs. 21 and 23 become equivalent. From this analogy, we consider that this N^0_{slide}/N_0 is related to this η. As illustrated in Fig. S8(a) in the Supporting Information, Mooney-Rivlin plots for SR gels exhibit a decay that closely matches the model curve under the assumption $\eta = N^0_{\mathrm{slide}}/N_0$, whereas the FC gels show almost no decay ($\eta = 0$). From these results, we conclude that SR gels behave similarly to networks with trapped entanglements, with N^0_{slide}/N_0 being analogous to η.

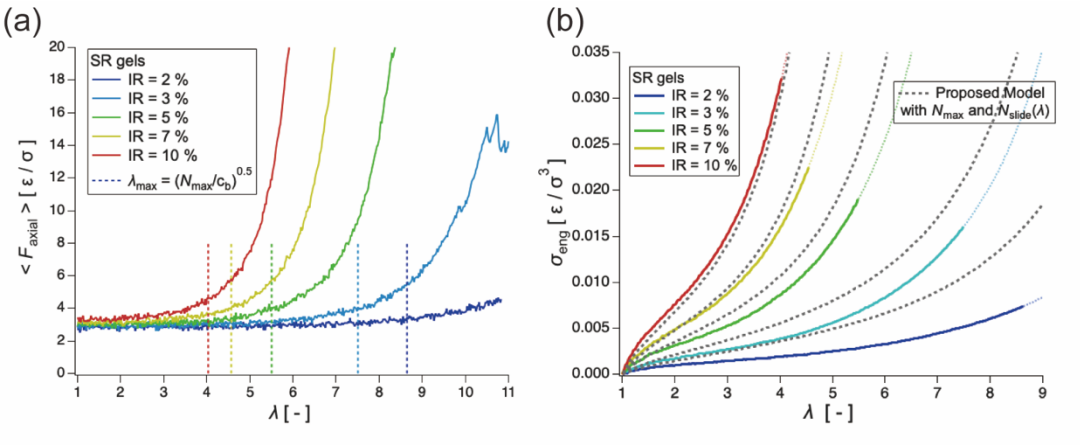

Fig. 11 (a) $<F_{axial}>$ plotted against λ. Dotted lines show the estimated values of $\lambda_{max} = (N_{max}/c_b)^{0.5}$. (b) σ_{eng}–λ curves of SR gels, along with the model lines predicted by Eq. 26 (dashed lines). The entropy elasticity region defined as $\lambda < \lambda_{max}$ is shown as solid lines; the non-entropic elasticity region is depicted as colored dotted lines.

Behavior at large deformation

Under large deformation, N_{max} becomes a dominant parameter. The deformation ratio corresponding to the fully extended state of a Kremer–Grest single chain with a bead number of N_{max} (λ_{max}) is given by:

$$\lambda_{max} = \frac{l_b N_{max}}{<R>} = \frac{l_b N_{max}}{l_b c_b \left(\frac{N_{max}}{c_b}\right)^{0.5}} = \left(\frac{N_{max}}{c_b}\right)^{0.5}. \quad (24)$$

Here, l_b is the average bond length (0.965σ[53]), $<R>$ is the average end-to-end length, and c_b is the number of beads per Kuhn length. By indicating this λ_{max} with $<F_{axial}>$, it was clarified that λ_{max} corresponds to the transition point between entropy- and energy-driven elasticity regimes discussed in Section 3.1. To capture strain-hardening behavior driven by entropy elasticity (solid lines in Fig. 11(b)), we modified the Treloar model (based on the inverse Langevin equation[45,54]).

In Treloar's finite extensibility model with inverse-Langevin function[45] (Eq. 25) the stress-elongation ratio relationship is written as:

$$\sigma_{\mathrm{eng}}(\lambda) = G\left(\lambda - \frac{1}{\lambda^2}\right) \left(1 + \frac{3}{25(N_0/c_\mathrm{b})}\left(3\lambda^2 + \frac{4}{\lambda}\right) + \frac{297}{6125(N_0/c_\mathrm{b})^2}\left(5\lambda^4 + 8\lambda + \frac{8}{\lambda^2}\right) + \frac{12312}{2205000(N_0/c_\mathrm{b})^3}\left(35\lambda^6 + 60\lambda^3 + 72 + \frac{64}{\lambda^3}\right) + \frac{126117}{693(673750)(N_0/c_\mathrm{b})^4}\left(630\lambda^8 + 1120\lambda^5 + 1440\lambda^2 + \frac{1536}{\lambda} + \frac{1280}{\lambda^4}\right) + \ldots \right) \quad (25)$$

Here, G is the shear modulus predicted from affine network model, N_0 is network strand length, and c_b is the Kuhn length (1.9σ[53] in Kremer-Grest model without stiffness ($\kappa \sim 0$)). In the previous section, it is confirmed that shear modulus of SR gels can be expressed as $G_{\mathrm{SR}} = G\left(1 - \frac{N^0_{\mathrm{slide}}}{N_0}\right)^2 = \lim_{\lambda \to 1} G\left(1 - \frac{N_{\mathrm{slide}}(\lambda)}{N_0}\right)^2$. Consequently, we replaced G with $G\left(1 - \frac{N_{\mathrm{slide}}(\lambda)}{N_0}\right)^2$. We also substituted N_0 by maximum chain length N_{max} in order to account for the finite extensibility term (3rd term). This yields

$$\sigma_{\mathrm{eng}}(\lambda) = G_{\mathrm{affine}}\left(1 - \frac{N_{\mathrm{slide}}(\lambda)}{N_0}\right)^2\left(\lambda - \frac{1}{\lambda^2}\right) \left(1 + \frac{3}{25(N_{\mathrm{max}}/c_\mathrm{b})}\left(3\lambda^2 + \frac{4}{\lambda}\right) + \frac{297}{6125(N_{\mathrm{max}}/c_\mathrm{b})^2}\left(5\lambda^4 + 8\lambda + \frac{8}{\lambda^2}\right) + \frac{12312}{2205000(N_{\mathrm{max}}/c_\mathrm{b})^3}\left(35\lambda^6 + 60\lambda^3 + 72 + \frac{64}{\lambda^3}\right) + \frac{126117}{693(673750)(N_{\mathrm{max}}/c_\mathrm{b})^4}\left(630\lambda^8 + 1120\lambda^5 + 1440\lambda^2 + \frac{1536}{\lambda} + \frac{1280}{\lambda^4}\right) \right) \quad (26)$$

Where $N_{\mathrm{slide}}(\lambda)$ is defined in Eq. 19. This model accurately reproduces the strain-hardening behavior of SR gels with IR of 7%, and 10% (Fig. 11(b)). For gels with lower IRs (2%, 3% and 5%), however, the theoretical σ_{eng}–λ curves overestimate the simulated data because strain

softening[29] (also shown in Fig. S4, S8 in the Supporting Information) occurs before strain hardening. This softening is not captured in the Treloar's model. Nonetheless, the strain-hardening behavior is well described by Eq. 26, confirming that N_{max} governs the mechanical response at large strains.

5. Conclusion

In this study, we performed MD simulations to investigate the origin of toughness and high extensibility in SR gels under uniaxial elongation. First, we calculated the σ_{eng}–λ curves for SR and FC gels to validate the model. The Young's moduli of SR gels were found to be smaller than those of FC gels, whereas the hardening strain of SR gels was larger than that of FC gels, consistent with experimental observations.

We then analyzed the stress distribution along the polymer chains and their orientation relative to the stretching direction to uncover the molecular mechanics underlying the unique properties of SR gels. In FC gels, force chains were observed along the stretching direction, exhibiting percolation under finite elongation. In contrast, such force chains were absent in SR gels. Instead, forces in SR gels were uniformly dispersed, and chains exhibited a higher degree of orientation along the stretching direction than was the case in FC gels. This homogeneous chain deformation suppresses strain hardening at large strain and mitigates stress concentration, providing the molecular basis for the high toughness of SR gels.

To further analyze the highly stretched structure of SR gels, we examined the one-dimensional trajectories of rings and cross-links along the axial chains. From the partial chain length distribution of stretched SR gels, we observed that N_{long} and N_{short} increased and decreased, respectively, at a rate proportional to N_{slide} because of the sliding of cross-links. At the limit of extension, N_{long} reached N_{max}, and N_{short} approached zero because slide-ring cross-links became immobilized at the ends or kinks of polymer chains. N^0_{slide}, which characterizes the extent of chain

movement, correlate with the Young's modulus of SR gels through the relation $E_{SR} = E_{affine}(1-N^0_{slide}/N_0)^2$, as confirmed in our previous work[40].

In this study, we further explained the strain-hardening behavior in SR gels using another characteristic parameter, N_{max}, which represents the length of the long strand when the short strand is fully extracted. Based on the Gaussian chain approximation, we demonstrated that N_{max} is closely related to the finite extensibility of SR gels. As shown above, $N_{slide}(\lambda)$ and N_{max} are the dominant factors influencing the stress–strain response at small strain and stress divergence under large deformation, respectively. These findings provide a clear understanding of the molecular mechanisms responsible for stress homogenization and the soft mechanical responses of SR gels. This work establishes a foundation for designing SR gels with desirable mechanical properties, such as enhanced softness and toughness, for future applications.

Author contribution

KI conceptualized the research; YY, KM, MT and HM developed the methodology; YY and TM conducted the investigation; YY performed the visualization; KM and KI supervised the study; YY wrote the original draft; and YY, TM, KM, MT, HY, HM, and KI reviewed and edited the manuscript.

Acknowledgements

This work was supported by Grants-in-Aid for Young Scientists (No. 15K17905 and 22K14740), Grants-in-Aid for Young Scientists (20J12541), AIST-UTokyo Advanced Operando-Measurement Technology Open Innovation Laboratory (OPERANDO-OIL), JST-Mirai Program (Grant No. JPMJMI18A2), JST CREST (Grant No. JPMJCR1992), and the Materials Education Program for the Future Leaders in Research, Industry, and Technology (MERIT). All calculations were conducted using the supercomputing system of the Institute for Solid State Physics (ISSP) (Project No. H29-Ba-0029, H30-Ba-0017, and H31-Ba-0015, 2022-Ba-18) and by Oakbridge-CX

in the Supercomputing Division, Information Technology Center, the University of Tokyo (Project code: gm79). The authors thank Prof. Shinji Tsuneyuki for his helpful comments and discussion. We thank Natasha Lundin, PhD, from Edanz (https://jp.edanz.com/ac) for editing a draft of this manuscript.

References

1 K. Y. Lee and D. J. Mooney, Hydrogels for Tissue Engineering, *Chem. Rev.*, 2001, **101**, 1869–1880.

2 A. Kidane, J. M. Szabocsik and K. Park, Accelerated study on lysozyme deposition on poly(HEMA) contact lenses, *Biomaterials*, 1998, **19**, 2051–2055.

3 K. Hayashi, F. Okamoto, S. Hoshi, T. Katashima, D. C. Zujur, X. Li, M. Shibayama, E. P. Gilbert, U. Chung, S. Ohba, T. Oshika and T. Sakai, Fast-forming hydrogel with ultralow polymeric content as an artificial vitreous body, *Nat Biomed Eng*, 2017, **1**, 0044.

4 M. Shibayama, Small-angle neutron scattering on polymer gels: phase behavior, inhomogeneities and deformation mechanisms, *Polym J*, 2011, **43**, 18–34.

5 K. Aomura, Y. Yasuda, T. Yamada, T. Sakai and K. Mayumi, Quasi-elastic neutron scattering study on dynamics of polymer gels with controlled inhomogeneity under uniaxial deformation, *Soft Matter*, 2023, **19**, 147–152.

6 J. P. Gong, Y. Katsuyama, T. Kurokawa and Y. Osada, Double-Network Hydrogels with Extremely High Mechanical Strength, *Advanced Materials*, 2003, **15**, 1155–1158.

7 J. P. Gong, Why are double network hydrogels so tough?, *Soft Matter*, 2010, **6**, 2583.

8 K. Imato, A. Takahara and H. Otsuka, Self-Healing of a Cross-Linked Polymer with Dynamic Covalent Linkages at Mild Temperature and Evaluation at Macroscopic and Molecular Levels, *Macromolecules*, 2015, **48**, 5632–5639.

9 J. Guo, R. Long, K. Mayumi and C.-Y. Hui, Mechanics of a Dual Cross-Link Gel with Dynamic Bonds: Steady State Kinetics and Large Deformation Effects, *Macromolecules*, 2016, **49**, 3497–3507.

10 S. Yoshida, H. Ejima and N. Yoshie, Tough Elastomers with Superior Self-Recoverability Induced by Bioinspired Multiphase Design, *Adv Funct Materials*, 2017, **27**, 1701670.

11 X. Huang, S. Nakagawa, H. Houjou and N. Yoshie, Insights into the Role of Hydrogen Bonds on the Mechanical Properties of Polymer Networks, *Macromolecules*, 2021, **54**, 4070–4080.

12 C. Kim, S. Nakagawa, M. Seshimo, H. Ejima, H. Houjou and N. Yoshie, Tough Supramolecular Elastomer via Entropy-Driven Hydrogen Bonds between Vicinal Diols, *Macromolecules*, 2020, **53**, 4121–4125.

13 Y. Yasuda, S. Nakagawa, H. Houjou, N. Yoshie and H. Morita, Coarse-Grained Molecular

Dynamics Simulations of Dynamic Bond Elastomers Using Interbead Potentials for Entropy- and Enthalpy-Driven Mechanisms in Their Dynamics and Mechanical Properties, *Macromolecules*, 2023, **56**, 7432–7444.

14 K. Urayama, T. Kawamura and S. Kohjiya, Elastic modulus and equilibrium swelling of networks crosslinked by end-linking oligodimethylsiloxane at solution state, *The Journal of Chemical Physics*, 1996, **105**, 4833–4840.

15 K. Urayama, T. Kawamura and S. Kohjiya, Structure–mechanical property correlations of model siloxane elastomers with controlled network topology, *Polymer*, 2009, **50**, 347–356.

16 T. Sakai, T. Matsunaga, Y. Yamamoto, C. Ito, R. Yoshida, S. Suzuki, N. Sasaki, M. Shibayama and U. Chung, Design and Fabrication of a High-Strength Hydrogel with Ideally Homogeneous Network Structure from Tetrahedron-like Macromonomers, *Macromolecules*, 2008, **41**, 5379–5384.

17 T. Fujiyabu, N. Sakumichi, T. Katashima, C. Liu, K. Mayumi, U. Chung and T. Sakai, Tri-branched gels: Rubbery materials with the lowest branching factor approach the ideal elastic limit, *Sci. Adv.*, 2022, **8**, eabk0010.

18 S. Nakagawa, D. Aoki, Y. Asano and N. Yoshie, Module-Assembled Elastomer Showing Large Strain Stiffening Capability and High Stretchability, *Advanced Materials*, 2023, **35**, 2301124.

19 X. Li, S. Nakagawa, Y. Tsuji, N. Watanabe and M. Shibayama, Polymer gel with a flexible and highly ordered three-dimensional network synthesized via bond percolation, *Sci. Adv.*, 2019, **5**, eaax8647.

20 T. Matsunaga, T. Sakai, Y. Akagi, U. Chung and M. Shibayama, Structure Characterization of Tetra-PEG Gel by Small-Angle Neutron Scattering, *Macromolecules*, 2009, **42**, 1344–1351.

21 T. Matsunaga, T. Sakai, Y. Akagi, U. Chung and M. Shibayama, SANS and SLS Studies on Tetra-Arm PEG Gels in As-Prepared and Swollen States, *Macromolecules*, 2009, **42**, 6245–6252.

22 Y. Okumura and K. Ito, The Polyrotaxane Gel: A Topological Gel by Figure-of-Eight Cross-links, *Adv. Mater.*, 2001, **13**, 485–487.

23 K. Mayumi, K. Ito and K. Kato, *Polyrotaxane and Slide-Ring Materials*, The Royal Society of Chemistry, 2015.

24 K. Ito, Novel Cross-Linking Concept of Polymer Network: Synthesis, Structure, and Properties of Slide-Ring Gels with Freely Movable Junctions, *Polym J*, 2007, **39**, 489–499.

25 A. Harada, J. Li and M. Kamachi, The molecular necklace: a rotaxane containing many threaded α-cyclodextrins, *Nature*, 1992, **356**, 325–327.

26 A. Harada, Y. Takashima and H. Yamaguchi, Cyclodextrin-based supramolecular polymers, *Chem. Soc. Rev.*, 2009, **38**, 875.

27 C. Liu, H. Kadono, K. Mayumi, K. Kato, H. Yokoyama and K. Ito, Unusual Fracture Behavior of Slide-Ring Gels with Movable Cross-Links, *ACS Macro Lett.*, 2017, **6**, 1409–1413.

28 L. Jiang, C. Liu, K. Mayumi, K. Kato, H. Yokoyama and K. Ito, Highly Stretchable and Instantly

Recoverable Slide-Ring Gels Consisting of Enzymatically Synthesized Polyrotaxane with Low Host Coverage, *Chem. Mater.*, 2018, **30**, 5013–5019.

29 C. Liu, K. Mayumi, K. Hayashi, L. Jiang, H. Yokoyama and K. Ito, Direct Observation of Large Deformation and Fracture Behavior at the Crack Tip of Slide-Ring Gel, *J. Electrochem. Soc.*, 2019, **166**, B3143–B3147.

30 C. Liu, N. Morimoto, L. Jiang, S. Kawahara, T. Noritomi, H. Yokoyama, K. Mayumi and K. Ito, Tough hydrogels with rapid self-reinforcement, *Science*, 2021, **372**, 1078–1081.

31 K. Hashimoto, T. Shiwaku, H. Aoki, H. Yokoyama, K. Mayumi and K. Ito, Strain-induced crystallization and phase separation used for fabricating a tough and stiff slide-ring solid polymer electrolyte, *Sci. Adv.*, 2023, **9**, eadi8505.

32 K. Ito, Novel entropic elasticity of polymeric materials: why is slide-ring gel so soft?, *Polym J*, 2012, **44**, 38–41.

33 Y. Yasuda, Y. Hidaka, K. Mayumi, T. Yamada, K. Fujimoto, S. Okazaki, H. Yokoyama and K. Ito, Molecular Dynamics of Polyrotaxane in Solution Investigated by Quasi-Elastic Neutron Scattering and Molecular Dynamics Simulation: Sliding Motion of Rings on Polymer, *J. Am. Chem. Soc.*, 2019, **141**, 9655–9663.

34 T. Karino, Y. Okumura, C. Zhao, T. Kataoka, K. Ito and M. Shibayama, SANS Studies on Deformation Mechanism of Slide-Ring Gel, *Macromolecules*, 2005, **38**, 6161–6167.

35 Y. Shinohara, K. Kayashima, Y. Okumura, C. Zhao, K. Ito and Y. Amemiya, Small-Angle X-ray Scattering Study of the Pulley Effect of Slide-Ring Gels, *Macromolecules*, 2006, **39**, 7386–7391.

36 K. Kato, Y. Ikeda and K. Ito, Direct Determination of Cross-Link Density and Its Correlation with the Elastic Modulus of a Gel with Slidable Cross-Links, *ACS Macro Lett.*, 2019, **8**, 700–704.

37 D. Chen, S. Panyukov, L. Sapir and M. Rubinstein, Elasticity of Slide-Ring Gels, *ACS Macro Lett.*, 2023, **12**, 362–368.

38 T. Koga and F. Tanaka, Elastic properties of polymer networks with sliding junctions, *Eur. Phys. J. E*, 2005, **17**, 225–229.

39 A. A. Gavrilov and I. I. Potemkin, Adaptive structure of gels and microgels with sliding cross-links: enhanced softness, stretchability and permeability, *Soft Matter*, 2018, **14**, 5098–5105.

40 Y. Yasuda, T. Masumoto, K. Mayumi, M. Toda, H. Yokoyama, H. Morita and K. Ito, Molecular Dynamics Simulation and Theoretical Model of Elasticity in Slide-Ring Gels, *ACS Macro Lett.*, 2020, **9**, 1280–1285.

41 K. Tanahashi and T. Koga, Molecular Simulation and Theoretical Analysis of Slide-Ring Gels under Biaxial Deformation, *Gels*, 2021, **7**, 129.

42 S. Uehara, Y. Wang, Y. Ootani, N. Ozawa and M. Kubo, Molecular-Level Elucidation of a Fracture Process in Slide-Ring Gels via Coarse-Grained Molecular Dynamics Simulations, *Macromolecules*, 2022, **55**, 1946–1956.

43 Y. Yasuda, M. Toda, K. Mayumi, H. Yokoyama, H. Morita and K. Ito, Sliding Dynamics of Ring on Polymer in Rotaxane: A Coarse-Grained Molecular Dynamics Simulation Study, *Macromolecules*, 2019, **52**, 3787–3793.

44 W. Kuhn, Über die Gestalt fadenförmiger Moleküle in Lösungen, *Kolloid-Zeitschrift*, 1934, **68**, 2–15.

45 L. R. G. Treolar, *The physics of rubber elasticity*, Oxford university press, New York, 3rd ed., 2005.

46 E. R. Duering, K. Kremer and G. S. Grest, Relaxation of randomly cross-linked polymer melts, *Phys. Rev. Lett.*, 1991, **67**, 3531–3534.

47 J. A. F. Chemical Innovation, Ed., *Computer Simulation of Polymeric Materials: Applications of the OCTA System*, Springer Singapore, Singapore, 2016.

48 A. P. Thompson, H. M. Aktulga, R. Berger, D. S. Bolintineanu, W. M. Brown, P. S. Crozier, P. J. In 'T Veld, A. Kohlmeyer, S. G. Moore, T. D. Nguyen, R. Shan, M. J. Stevens, J. Tranchida, C. Trott and S. J. Plimpton, LAMMPS - a flexible simulation tool for particle-based materials modeling at the atomic, meso, and continuum scales, *Computer Physics Communications*, 2022, **271**, 108171.

49 J. Gao and J. H. Weiner, Monomer-Level Description of Stress and Birefringence Relaxation in Polymer Melts, *Macromolecules*, 1994, **27**, 1201–1209.

50 L. R. G. Treloar, The photoelastic properties of short-chain molecular networks, *Trans. Faraday Soc.*, 1954, **50**, 881.

51 R. C. Ball, M. Doi, S. F. Edwards and M. Warner, Elasticity of entangled networks, *Polymer*, 1981, **22**, 1010–1018.

52 S. F. Edwards and Th. Vilgis, The effect of entanglements in rubber elasticity, *Polymer*, 1986, **27**, 483–492.

53 R. Everaers, H. A. Karimi-Varzaneh, F. Fleck, N. Hojdis and C. Svaneborg, Kremer–Grest Models for Commodity Polymer Melts: Linking Theory, Experiment, and Simulation at the Kuhn Scale, *Macromolecules*, 2020, **53**, 1901–1916.

54 M. Rubinstein and R. H. Colby, *Polymer physics*, Oxford Univ. Press, Oxford, repr., 2014.

Data Availability Statement for:

Coarse-Grained Molecular Dynamics Simulations of Slide-ring Gels under Finite Deformation: Influence of Sliding Ring Rearrangement on Softness and Extensibility

Data Availability:

All data needed to run the same calculation and evaluate the conclusions in the Paper are present in the Paper and the Supporting Information. Codes are available from the corresponding author upon reasonable request.